SCIENCE CHINA
Technological Sciences

October 2013 Vol.56 No.10: 2370–2384
doi: 10.1007/s11431-013-5334-y

A high-order multidimensional gas-kinetic scheme for hydrodynamic equations

LUO Jun & XU Kun*

Mathematics Department, Hong Kong University of Science and Technology, Clear Water Bay, Kowloon, Hong Kong, China

Received June 29, 2013; accepted August 13, 2013; published online September 9, 2013

This paper concerns the development of high-order multidimensional gas kinetic schemes for the Navier-Stokes solutions. In the current approach, the state-of-the-art WENO-type initial reconstruction and the gas-kinetic evolution model are used in the construction of the scheme. In order to distinguish the physical and numerical requirements to recover a physical solution in a discretized space, two particle collision times will be used in the current high-order gas-kinetic scheme (GKS). Different from the low order gas dynamic model of the Riemann solution in the Godunov type schemes, the current method is based on a high-order multidimensional gas evolution model, where the space and time variation of a gas distribution function along a cell interface from an initial piecewise discontinuous polynomial is fully used in the flux evaluation. The high-order flux function becomes a unification of the upwind and central difference schemes. The current study demonstrates that both the high-order initial reconstruction and high-order gas evolution model are important in the design of a high-order numerical scheme. Especially, for a compact method, the use of a high-order local evolution solution in both space and time may become even more important, because a short stencil and local low order dynamic evolution model, i.e., the Riemann solution, are contradictory, where valid mechanism for the update of additional degrees of freedom becomes limited.

WENO reconstruction, gas-kinetic schemes, Euler, Navier-Stokes, high-order methods

Citation: Luo J, Xu K. A high-order multidimensional gas-kinetic scheme for hydrodynamic equations. Sci China Tech Sci, 2013, 56: 2370–2384, doi: 10.1007/ s11431-013-5334-y

1 Introduction

Following the essentially non-oscillatory (ENO) scheme introduced by Harten et al. in 1987 [1, 2], the weighted essentially non-oscillatory (WENO) scheme was further developed in the construction of high-order numerical scheme for hyperbolic conservation laws [3, 4]. The basic idea of the WENO technique is a convex linear combination of lower order reconstructions to obtain a higher-order approximation. The WENO reconstruction is very effective in both controlling the oscillation and restoring smooth distribution. The WENO schemes may be used for the flux reconstruction as well.

In the past years, a gas-kinetic scheme (GKS) has been developed for the Euler and Navier-Stokes (NS) solutions [5−7]. Theoretically, GKS does not target to solve the gas kinetic BGK equation [8], but uses it to construct a gas evolution process from a piecewise discontinuous initial data for the flux evaluation in a finite volume scheme. Only in the limiting case, such as in the smooth flow region, the NS solution with correct Prandtl number can be recovered from the kinetic gas evolution model. In the discontinuous case, the whole process from the particle free transport to the NS or Euler solution construction has been recovered in the gas-kinetic solution. In the smooth flow region, the NS solution for the viscous flow or the Euler solution for the inviscid flow can be obtained accurately by GKS. In the

*Corresponding author (email: makxu@ust.hk)

discontinuity region where the solution cannot be well resolved in a discretized space, it is hard to identify which governing equation is solved in the gas evolution modeling. Theoretically, for the unresolved flow region the solution is not unique. In such a region, we only need to impose that the numerical evolution path is consistent with a physical one, such as keeping a non-equilibrium distribution function for providing enough numerical dissipation. Actually, a correct numerical modeling is the key to avoid the so-called shock instability in high Mach number cases, such as the carbuncle phenomena [9].

The combination of the WENO reconstruction and gas-kinetic flux formulation has been recently done for turbulent simulations [10]. The scheme presented in ref. [10] is based on a 2nd-order kinetic flux function [6]. In this paper, as an extension from the previous directional splitting 3rd-order gas-kinetic scheme [11], we are going to construct a multi-dimensional high-order scheme by following the time evolution from a WENO-type initial data. The integral solution of the gas-kinetic model will be constructed from a piecewise discontinuous high-order initial condition. In order to distinguish the physical and numerical requirements to recover a physical solution in a discretized space, two particle collision times, which control the evolution process from a non-equilibrium to an equilibrium state, will be used in the current high-order GKS. A distinguishable particle collision time helps to keep a high-order solution in the smooth flow region, and to control numerical oscillations efficiently around a shock discontinuity. In the well resolved flow regions, the current scheme presents an accurate NS or Euler solution. In the under-resolved discontinuity region, the gas evolution process from free particle transport to the NS solution provides an adequate numerical dissipation. In the current scheme, all high-order spatial derivatives will participate in the construction of a space and time dependent flux function. The new scheme presented in this paper is named WENO-gas-kinetic scheme (WENO-GKS).

This paper is organized as follows. Section 2 is the construction of high-order multidimensional scheme. Section 3 is the WENO reconstruction, followed by the numerical experiments in Section 4. The last section draws the conclusions.

2 A high-order multidimensional flow solver

The gas-kinetic BGK equation in 2D case is

$$f_t + \boldsymbol{u}\cdot\nabla f = \frac{g-f}{\tau}, \tag{1}$$

where f is the gas distribution function and g is the equilibrium distribution function approached by f, ∇f is the gradient of f with respect to $\boldsymbol{x}$, $\boldsymbol{x}$ = (x, y), and $\boldsymbol{u}$ = (u, v) is the particle velocity. The particle collision time τ is related to the viscosity and heat conduction coefficients, i.e., $\tau = \mu/p$ where μ is the dynamic viscosity coefficient and p is the pressure. The relation between the macroscopic quantities, mass ρ, momentum (ρU, ρV), and energy ρE, and the distribution function f is

$$W = \int\int\int \psi f \mathrm{d}u\mathrm{d}v\mathrm{d}\xi, \tag{2}$$

where $W = (\rho,\ \rho U,\ \rho V,\ \rho E)^{\mathrm{T}}$, ($U$, V) is the macroscopic velocity of the fluid,

$$\psi = (\psi_1,\psi_2,\psi_3,\psi_4)^{\mathrm{T}} = (1,u,v,\frac{1}{2}(u^2+v^2+\xi^2))^{\mathrm{T}},$$

$\mathrm{d}\xi = \mathrm{d}\xi_1\mathrm{d}\xi_2...\mathrm{d}\xi_K$, and K is the number of degrees of internal freedom, i.e., $K = (4-2\gamma)/(\gamma-1)$ for 2D flow and γ is the specific heat ratio. Since the mass, momentum, and energy are conserved during particle collisions, f and g satisfy the conservation constraint,

$$\int\int\int (g-f)\psi_\alpha \mathrm{d}u\mathrm{d}v\mathrm{d}\xi = 0, \quad \alpha = 1,2,3,4, \tag{3}$$

at any point in space and time. The integral solution of eq. (1) is

$$f(\boldsymbol{x},t,\boldsymbol{u},\xi) = \frac{1}{\tau}\int_0^t g(\boldsymbol{x}',t',\boldsymbol{u},\xi)\mathrm{e}^{-(t-t')/\tau}\mathrm{d}t' + \mathrm{e}^{-t/\tau} f_0(\boldsymbol{x}-\boldsymbol{u}t,\boldsymbol{u},\xi), \tag{4}$$

where $\boldsymbol{x}' = \boldsymbol{x} - \boldsymbol{u}(t-t')$ is the particle trajectory. The solution f in eq. (4) solely depends on the modeling of f_0 and g. So, besides the above kinetic solution, a numerical modeling with valid physical foundation is the key for the success of the gas-kinetic scheme.

In the modeling of initial f_0, a proper choice is the NS gas distribution function, which can be obtained from eq. (1) through the Chapman-Enskog expansion. In the smooth flow region, the Chapman-Enskog expansion gives a solution

$$f_{\mathrm{G}}(\boldsymbol{x},t,\boldsymbol{u},\xi) = g(\boldsymbol{x},t,\boldsymbol{u},\xi) + \tau\Phi_1(\boldsymbol{x},t,\boldsymbol{u},\xi) + \tau^2\Phi_2(\boldsymbol{x},t,\boldsymbol{u},\xi) + \cdots. \tag{5}$$

By truncating the solution to different orders of τ, we can get different macroscopic governing equations. The relations between the approximated solutions and the macroscopic equations are [12],

$$f_{\mathrm{G}}(\boldsymbol{x},t,\boldsymbol{u},\xi) = g(\boldsymbol{x},t,\boldsymbol{u},\xi) + O(\tau) \leftrightarrow \text{Euler quations},$$

$$f_{\mathrm{G}}(\boldsymbol{x},t,\boldsymbol{u},\xi) = g(\boldsymbol{x},t,\boldsymbol{u},\xi) + \tau\Phi_1(\boldsymbol{x},t,\boldsymbol{u},\xi) + O(\tau^2) \leftrightarrow \text{Navier-Stokes equations},$$

$$f_{\mathrm{G}}(\boldsymbol{x},t,\boldsymbol{u},\xi) = g(\boldsymbol{x},t,\boldsymbol{u},\xi) + \tau\Phi_1(\boldsymbol{x},t,\boldsymbol{u},\xi) + \tau^2\Phi_2(\boldsymbol{x},t,\boldsymbol{u},\xi) + O(\tau^3) \leftrightarrow \text{Burnett equations}.$$

……

In this paper, we only consider the Euler and NS solutions, which correspond to

$$f_{\mathrm{Eu}}(\boldsymbol{x},t,\boldsymbol{u},\xi)=g(\boldsymbol{x},t,\boldsymbol{u},\xi), \tag{6}$$

$$f_{\mathrm{NS}}(\boldsymbol{x},t,\boldsymbol{u},\xi)=g(\boldsymbol{x},t,\boldsymbol{u},\xi)-\tau[g_t(\boldsymbol{x},t,\boldsymbol{u},\xi)+\boldsymbol{u}\cdot\nabla g(\boldsymbol{x},t,\boldsymbol{u},\xi)], \tag{7}$$

where the non-equilibrium part is defined by

$$\Phi_1(\boldsymbol{x},t,\boldsymbol{u},\xi)=-[g_t(\boldsymbol{x},t,\boldsymbol{u},\xi)+\boldsymbol{u}\cdot\nabla g(\boldsymbol{x},t,\boldsymbol{u},\xi)].$$

2.1 Taylor expansion of a gas distribution function

In the construction of GKS, an expansion of a gas distribution function in space and time is needed. Assume that the expansion point is $\boldsymbol{x}=(0,0)$. A 3rd-order Taylor expansion of a gas distribution function becomes

$$\begin{aligned}&f_{\mathrm{L}}(\boldsymbol{x},t)\\&=f_{\mathrm{G}}(0,0,0)+\frac{\partial f_{\mathrm{G}}}{\partial x}|_{(0,0,0)}\ x+\frac{\partial f_{\mathrm{G}}}{\partial y}|_{(0,0,0)}\ y\\&+\frac{\partial f_{\mathrm{G}}}{\partial t}|_{(0,0,0)}\ t+\frac{1}{2}\frac{\partial^2 f_{\mathrm{G}}}{\partial x^2}|_{(0,0,0)}\ x^2+\frac{1}{2}\frac{\partial^2 f_{\mathrm{G}}}{\partial y^2}|_{(0,0,0)}\ y^2\\&+\frac{\partial^2 f_{\mathrm{G}}}{\partial x\partial y}|_{(0,0,0)}\ xy+\frac{1}{2}\frac{\partial^2 f_{\mathrm{G}}}{\partial t^2}|_{(0,0,0)}\ t^2\\&+\frac{\partial^2 f_{\mathrm{G}}}{\partial x\partial t}|_{(0,0,0)}\ xt+\frac{\partial^2 f_{\mathrm{G}}}{\partial y\partial t}|_{(0,0,0)}\ yt.\end{aligned} \tag{8}$$

Here, the expansion is in the (x, y, t) physical space, where the phase space variables ($\boldsymbol{u}$, ξ) of particle velocity do not appear. Besides the above expansion in space and time, we may need the expansion along a cell interface as well. Without losing generality, assume that the x-direction is the normal direction and the y-direction is the tangential direction of a cell interface. For a 3rd-order scheme, along the cell interface the expansion of the distribution function becomes

$$\begin{aligned}f(0,y,t)&=f_{\mathrm{L}}(0,y,t)\\&=f_{\mathrm{G}}(0,0,0)+\frac{\partial f_{\mathrm{G}}}{\partial y}|_{(0,0,0)}\ y+\frac{\partial f_{\mathrm{G}}}{\partial t}|_{(0,0,0)}\ t\\&+\frac{1}{2}\frac{\partial^2 f_{\mathrm{G}}}{\partial y^2}|_{(0,0,0)}\ y^2+\frac{1}{2}\frac{\partial^2 f_{\mathrm{G}}}{\partial t^2}|_{(0,0,0)}\ t^2\\&+\frac{\partial^2 f_{\mathrm{G}}}{\partial y\partial t}|_{(0,0,0)}\ yt.\end{aligned} \tag{9}$$

The above expansion will be used to model f_0 in the integral solution (4) at the cell interface. When $f_{\mathrm{G}}=f_{\mathrm{Eu}}$ or $f_{\mathrm{G}}=f_{\mathrm{NS}}$ is substituted into the above equations, the expansion of the Euler or NS solution can be recovered.

For convenience, some notations will be introduced first,

$$g_0=g(0,0,0),a_1=\left(\frac{\partial g}{\partial x}/\,g\right)|_{(0,0,0)},$$

$$a_2=\left(\frac{\partial g}{\partial y}/\,g\right)|_{(0,0,0)},\ A=\left(\frac{\partial g}{\partial t}/\,g\right)|_{(0,0,0)},$$

$$d_{11}=\frac{\partial a_1}{\partial x}|_{(0,0,0)},d_{22}=\frac{\partial a_2}{\partial y}|_{(0,0,0)},\ d_{12}=\frac{\partial a_1}{\partial y}|_{(0,0,0)}=\frac{\partial a_2}{\partial x}|_{(0,0,0)},$$

$$b_1=\frac{\partial a_1}{\partial t}|_{(0,0,0)}=\frac{\partial A}{\partial x}|_{(0,0,0)},\ b_2=\frac{\partial a_2}{\partial t}|_{(0,0,0)}=\frac{\partial A}{\partial y}|_{(0,0,0)},$$

$$B=\frac{\partial A}{\partial t}|_{(0,0,0)}.$$

In the above formulations, g_0 is the Maxwellian distribution function, which can be obtained from macroscopic flow variables $W=(\rho,\ (\rho U),\ (\rho V),\ (\rho E))^{\mathrm{T}}$ at $\boldsymbol{x}$ = (0, 0). The equilibrium state is denoted by

$$g_0=\rho\left(\frac{\lambda}{\pi}\right)^{\frac{K+2}{2}}\mathrm{e}^{\lambda((u-U)^2+(v-V)^2+\xi^2)}, \tag{10}$$

where λ equals to $m/2kT$, m is the molecular mass, k is the Boltzmann constant, and T is the temperature.

2.2 A kinetic solver for fully continuous case

In the smooth flow region, with a continuous flow distribution across a cell interface any high-order scheme should be able to recover the traditional high-order central difference method. Here, we provide such a benchmark limiting solution, which helps the design of high-order scheme in general discontinuous case. In other words, the general formulation from a discontinuous initial data should be able to recover the smooth flow solution in case of the continuity.

For a continuous flow distribution across a cell interface, eq. (9) provides a high-order space-time solution, which is beyond the traditional Lax-Wendroff scheme.

Continuous gas-kinetic Euler flow solver:

$$\begin{aligned}&f_{\mathrm{G}}=f_{\mathrm{Eu}}=g,\\&f(0,y,t,\boldsymbol{u},\xi)=g_0[1+a_2y+At+\frac{1}{2}(a_2^2+d_{22})y^2\\&+\frac{1}{2}(A^2+B)t^2+(Aa_2+b_2)yt].\end{aligned} \tag{11}$$

Continuous gas-kinetic NS flow solver:

$$\begin{aligned}&f_{\mathrm{G}}=f_{\mathrm{NS}}=g-\tau(ug_x+vg_y+g_t),\\&f(0,y,t,\boldsymbol{u},\xi)\\&=g_0[1-\tau(a_1u+a_2v+A)]\\&+g_0[a_2-\tau((a_1a_2+d_{12})u+(a_2^2+d_{22})v+Aa_2+b_2)]y\\&+g_0[A-\tau((Aa_1+b_1)u+(Aa_2+b_2)v+A^2+B)]t\\&+\frac{1}{2}g_0(a_2^2+d_{22})y^2+\frac{1}{2}g_0(A^2+B)t^2+g_0(Aa_2+b_2)yt.\end{aligned} \tag{12}$$

The above time and space dependent gas distribution

function f can be used for the evaluation of numerical fluxes across a cell interface. This can be considered as a generalized high-order Lax-Wendroff scheme for Euler and NS solutions.

2.3 Kinetic flow solver in discontinuous case

In general case, the reconstruction will introduce a discontinuity at the numerical cell interface. The distribution function expansion eq. (8) will be different on different sides of a cell interface. Therefore, the initial gas distribution function f_0 in the integral solution eq. (4) can be expanded separately,

$$f_0(\boldsymbol{x},\boldsymbol{u},\xi)=\begin{cases} f_0^l(\boldsymbol{x},\boldsymbol{u},\xi)=f_L^l(\boldsymbol{x},0,\boldsymbol{u},\xi), & x<0,\\ f_0^r(\boldsymbol{x},\boldsymbol{u},\xi)=f_L^r(\boldsymbol{x},0,\boldsymbol{u},\xi), & x>0, \end{cases} \tag{13}$$

where f_L^l and f_L^r still have the form of eq. (8), which can fully be determined from the reconstructed macroscopic variables, which is presented in the next subsection. For the modeling of the local equilibrium distribution function g in the integral solution eq. (4), we can also use the Taylor expansion and get

$$\begin{aligned} &g(\boldsymbol{x},t,\boldsymbol{u},\xi)\\ &=\overline{g}+\overline{g}a_1x+\overline{g}a_2y+\overline{g}\overline{A}t+\frac{1}{2}\overline{g}(a_1^2+d_{11})x^2\\ &+\frac{1}{2}\overline{g}(a_2^2+d_{22})y^2+\overline{g}(a_1a_2+d_{12})xy\\ &+\frac{1}{2}\overline{g}(\overline{A}^2+\overline{B})t^2+\overline{g}(\overline{A}a_1+b_1)xt+\overline{g}(\overline{A}a_2+b_2)yt, \end{aligned} \tag{14}$$

where $\overline{g}$ is the equilibrium state on the cell interface. Because of eq. (3), at $(\boldsymbol{x},t)=(0,0,0)$, $\overline{g}$ can be obtained from

$$\begin{aligned} \int\int\int \overline{g}\psi \mathrm{d}u\mathrm{d}v\mathrm{d}\xi=\overline{W}=&\iiint_{u>0} f_0^l(0,\boldsymbol{u},\xi)\psi \mathrm{d}u\mathrm{d}v\mathrm{d}\xi\\ &+\iiint_{u<0} f_0^r(0,\boldsymbol{u},\xi)\psi \mathrm{d}u\mathrm{d}v\mathrm{d}\xi. \end{aligned} \tag{15}$$

The other parameters in eq. (14) will be determined from the macroscopic flow distributions across a cell interface, which will be presented in the next subsection.

After determining f_0 and g, the time dependent distribution function along a cell interface is given by the integral solution eq. (4). Since the integral solution may go to the Burnett order as well, in order to recover the Euler or NS solution precisely the smooth limiting solution in Subsection 2.2 will be used to selectively remove some terms in the integration solution,

$$\int_0^t g(\boldsymbol{x}',t',\boldsymbol{u},\xi)\mathrm{e}^{-(t-t')/\tau}\mathrm{d}t'.$$

For the Euler solution, we need to delete the viscous terms as well. To remove certain terms is also one of the modeling processes for the development of GKS.

Based on the fully integral solution,

$$\begin{aligned} &f(0,y,t,\boldsymbol{u},\xi)\\ &=\frac{1}{\tau}\int_0^t g(-u(t-t'),y-v(t-t'),t',\boldsymbol{u},\xi)\mathrm{e}^{-(t-t')/\tau}\mathrm{d}t'\\ &+\mathrm{e}^{-t/\tau}f_0(-ut,y-vt,\boldsymbol{u},\xi), \end{aligned} \tag{16}$$

a high-order GKS-NS solver has the solution

$$\begin{aligned} &\frac{1}{\tau}\int_0^t g(-u(t-t'),y-v(t-t'),t',\boldsymbol{u},\xi)\mathrm{e}^{-(t-t')/\tau}\mathrm{d}t'\\ &=C_1\overline{g}+C_2\overline{g}a_1u+C_1\overline{g}a_2y+C_2\overline{g}a_2v+C_3\overline{g}\overline{A}\\ &+\frac{1}{2}C_4\overline{g}(a_1^2+d_{11})u^2+\frac{1}{2}C_1\overline{g}(a_2^2+d_{22})y^2\\ &+C_2\overline{g}(a_2^2+d_{22})vy+\frac{1}{2}C_4\overline{g}(a_2^2+d_{22})v^2\\ &+C_2\overline{g}(a_1a_2+d_{12})uy+C_4\overline{g}(a_1a_2+d_{12})uv\\ &+\frac{1}{2}C_5\overline{g}(\overline{A}^2+\overline{B})+C_6\overline{g}(\overline{A}a_1+b_1)u\\ &+C_3\overline{g}(\overline{A}a_2+b_2)y+C_6\overline{g}(\overline{A}a_2+b_2)v, \end{aligned} \tag{17}$$

and

$$\begin{aligned} &\mathrm{e}^{-t/\tau}f_0(-ut,y-vt,\boldsymbol{u},\xi)\\ &=\begin{cases} \mathrm{e}^{-t/\tau}f_0^l(-ut,y-vt,\boldsymbol{u},\xi), & u>0,\\ \mathrm{e}^{-t/\tau}f_0^r(-ut,y-vt,\boldsymbol{u},\xi), & u<0, \end{cases} \end{aligned} \tag{18}$$

where

$$\begin{aligned} &\mathrm{e}^{-t/\tau}f_0^{l,r}(-ut,y-vt,\boldsymbol{u},\xi)\\ &=C_7g_0^{l,r}[1-\tau(a_1^{l,r}u+a_2^{l,r}v+A^{l,r})]\\ &+C_8g_0^{l,r}[a_1^{l,r}u-\tau(((a_1^{l,r})^2+d_{11}^{l,r})u^2\\ &+(a_1^{l,r}a_2^{l,r}+d_{12}^{l,r})uv+(A^{l,r}a_1^{l,r}+b_1^{l,r})u)]\\ &+C_7g_0^{l,r}[a_2^{l,r}-\tau((a_1^{l,r}a_2^{l,r}+d_{12}^{l,r})u\\ &+((a_2^{l,r})^2+d_{22}^{l,r})v+A^{l,r}a_2^{l,r}+b_2^{l,r})]y\\ &+C_8g_0^{l,r}[a_2^{l,r}v-\tau((a_1^{l,r}a_2^{l,r}+d_{12}^{l,r})uv\\ &+((a_2^{l,r})^2+d_{22}^{l,r})v^2+(A^{l,r}a_2^{l,r}+b_2^{l,r})v)]\\ &+\frac{1}{2}C_9g_0^{l,r}((a_1^{l,r})^2+d_{11}^{l,r})u^2+\frac{1}{2}C_7g_0^{l,r}((a_2^{l,r})^2+d_{22}^{l,r})y^2\\ &+C_8g_0^{l,r}((a_2^{l,r})^2+d_{22}^{l,r})vy+\frac{1}{2}C_9g_0^{l,r}((a_2^{l,r})^2+d_{22}^{l,r})v^2\\ &+C_8g_0^{l,r}(a_1^{l,r}a_2^{l,r}+d_{12}^{l,r})uy+C_9g_0^{l,r}(a_1^{l,r}a_2^{l,r}+d_{12}^{l,r})uv. \end{aligned} \tag{19}$$

The coefficients are given by

$$\begin{aligned} &C_1=1-\mathrm{e}^{-t/\tau_n},\ \ C_2=(t+\tau)\mathrm{e}^{-t/\tau_n}-\tau,\\ &C_3=t-\tau+\tau\mathrm{e}^{-t/\tau_n},\ \ C_4=(-t^2-2\tau t)\mathrm{e}^{-t/\tau_n},\\ &C_5=t^2-2\tau t,\ \ C_6=-\tau t(1+\mathrm{e}^{-t/\tau_n}),\\ &C_7=\mathrm{e}^{-t/\tau_n},\ \ C_8=-t\mathrm{e}^{-t/\tau_n},\ \ C_9=t^2\mathrm{e}^{-t/\tau_n}. \end{aligned} \tag{20}$$

In the above equations, two collision times, i.e., τ and τ_{n}, are introduced. The numerical collision time τ_{n} controls the contributions from f_0 and g in the final integral solution in the discontinuous case. The physical one, i.e., $\tau = \mu/p$ and μ, captures the resolved dissipative NS solution. When $\tau = 0$, the above formulae give to the Euler solution.

In a numerical scheme, a discretized space provides limited resolution. As explained in ref. [6], there are two kinds of numerical dissipation, one is the kinematic dissipation coming from the initial reconstruction, and the other is the dynamical one in the gas evolution model. In GKS, starting from a discontinuity, the flow behavior depends on the ratio between the time passed and particle collision time. The integral solution eq. (16) describes such a relaxation process from the molecular free transport to the equilibrium state formation. In eq. (20), the term that controls the relaxation process from f_0 to g is $e^{-t/\tau_{\mathrm{n}}}$. Therefore, in order to introduce dynamical dissipation, the numerical collision time τ_{n} is defined with the consideration of cell size and artificial discontinuous jump. The collision time τ in other places represents the deviation from an equilibrium state, which keeps a physical value.

For the Euler solutions, the physical collision time τ should approach to zero in order to keep an equilibrium state everywhere. However, due to the limited cell resolution, such that the shock thickness should be on the order of cell size, the numerical collision time should take this into account,

$$\tau_{\mathrm{n}} = \alpha\Delta x\sqrt{\overline{\lambda}} + \beta\Delta x\sqrt{\overline{\lambda}}\,|\,p^l - p^r\,|/(p^l + p^r), \tag{21}$$

where α and β are two constant parameters, $\overline{\lambda}$ is given in the equilibrium state $\overline{g}$, and p^l and p^r are the pressure jump at the cell interface in the initially reconstructed data. For inviscid flow, as mesh size goes to zero, τ_{n} will go to zero as well, and GKS converges to the Euler solutions.

For the NS solutions, the physical collision time τ is related to the dynamical viscosity μ. Therefore, there are two collision times here. The physical collision time τ and the numerical one τ_{n} for the NS solution are defined by

$$\begin{aligned} &\tau = \mu/\overline{p}, \\ &\tau_{\mathrm{n}} = \mu/\overline{p} + \beta\Delta x\sqrt{\overline{\lambda}}\,|\,p^l - p^r\,|/(p^l + p^r), \end{aligned} \tag{22}$$

where $\overline{p}$ is the pressure in the equilibrium state $\overline{g}$.

2.4 Determination of expansion coefficients in the distribution function

In order to fully determine the gas distribution function at a cell interface, all coefficients, i.e., $a_1^l, a_1^r, a_1, \cdots, A^l, A^r, \overline{A}, \cdots$, must be given. Since all these coefficients are coming from the expansion of a Maxwellian, they should have one-to-one correspondence with the macroscopic variables and their derivatives. After initial reconstruction, we can get the macroscopic variables and their spatial derivatives on the left and right sides of a cell interface respectively. To sum up, the essential question is how to get the coefficients ($a_1, a_2, \cdots, A, B$), when the corresponding macroscopic variables $W = (\rho, (\rho U), (\rho V), (\rho E))^{\mathrm{T}}$ and their spatial derivatives are available.

From ref. [5] or [6], a coefficient Λ can be always written as $\Lambda = (\Lambda_1, \Lambda_2, \Lambda_3, \Lambda_4)\cdot\psi$. Assume g_0 is the Maxwellian corresponding to W, and

$$\langle\cdots\rangle = \int\int\int g_0(\cdots)\psi \mathrm{d}u\mathrm{d}v\mathrm{d}\xi,$$

then all the coefficients can be obtained by the following formulae which are directly derived from the conservation constraints eq. (3), such as

$$\begin{aligned} &\langle a_1\rangle = \frac{\partial W}{\partial x} \to a_1,\ \langle a_2\rangle = \frac{\partial W}{\partial y} \to a_2, \\ &\langle a_1^2 + d_{11}\rangle = \frac{\partial^2 W}{\partial x^2} \to d_{11},\ \langle a_2^2 + d_{22}\rangle = \frac{\partial^2 W}{\partial y^2} \to d_{22}, \\ &\langle a_1 a_2 + d_{12}\rangle = \frac{\partial^2 W}{\partial x\partial y} \to d_{12}, \langle a_1 u + a_2 v + A\rangle = 0 \to A, \\ &\langle (a_1^2 + d_{11})u + (a_1 a_2 + d_{12})v + A a_1 + b_1\rangle = 0 \to b_1, \\ &\langle (a_1 a_2 + d_{12})u + (a_2^2 + d_{22})v + A a_2 + b_2\rangle = 0 \to b_2, \\ &\langle (A a_1 + b_1)u + (A a_2 + b_2)v + A^2 + B\rangle = 0 \to B. \end{aligned}$$

2.5 Finite volume high-order multidimensional GKS

For a finite volume scheme, the fluxes across a cell interface need to be evaluated in order to update the cell-average conservative flow variables. In GKS, the fluxes are defined by

$$F = \int\int\int u\psi f \mathrm{d}u\mathrm{d}v\mathrm{d}\xi, \tag{23}$$

where the fluxes $F = (F_\rho, F_{\rho U}, F_{\rho V}, F_{\rho E})^{\mathrm{T}}$ depend on the gas distribution function f in eq. (16) at the cell interface. For a rectangular cell bounded by the straight lines, $x = x_{i-1/2}$, $x = x_{i+1/2}$, $y = y_{j-1/2}$ and $y = y_{j+1/2}$, the update of the cell-average conservative variables W_{ij} from time step t_n to t_{n+1} becomes

$$\begin{aligned} &W_{ij}^{n+1} \\ &= W_{ij}^{n} + \frac{1}{\Delta x_i \Delta y_j}\int_{t_n}^{t_{n+1}}\int_{-\frac{1}{2}\Delta x_i}^{\frac{1}{2}\Delta x_i}\left[F_{j-1/2}(t,x) - F_{j+1/2}(t,x)\right]\mathrm{d}x\mathrm{d}t \\ &+ \frac{1}{\Delta x_i \Delta y_j}\int_{t_n}^{t_{n+1}}\int_{-\frac{1}{2}\Delta y_j}^{\frac{1}{2}\Delta y_j}\left[F_{i-1/2}(t,y) - F_{i+1/2}(t,y)\right]\mathrm{d}y\mathrm{d}t, \end{aligned} \tag{24}$$

where $F_{j-1/2}(t,x), F_{j+1/2}(t,x), F_{i-1/2}(t,y), F_{i+1/2}(t,y)$ are the fluxes at the four cell interfaces respectively, $\Delta x_i = x_{i+1/2} - x_{i-1/2}$ and $\Delta y_j = y_{j+1/2} - y_{j-1/2}$. Note for each cell interface, the flux depends on the location along the interface. After integrating the fluxes in time and space along the cell boundary, a high-order GKS is obtained. The order of the scheme depends on the accuracy of the Taylor expansion in eq. (8). After increasing the accuracy of the Taylor expansion, an even higher-order accurate scheme can be constructed.

3 The 5th-order WENO subcell reconstruction

For GKS, all the reconstructions are based on the conservative variables. The formulation to get the pointwise values on the left and right hand sides of a cell interface is given in ref. [13]. Based on these pointwise values, a corresponding 3rd-order subcell reconstruction inside each cell is presented here.

3.1 The 5th-order WENO reconstruction on uniform structured mesh

Assume that Q is the variable that needs to be reconstructed. $\overline{Q}_i$ is the cell averaged value in the ith cell. Q_i^l and Q_i^r are the two values obtained from the reconstruction at the left and right interfaces of the ith cell. The 5th WENO reconstruction is defined as,

$$Q_i^r = \sum_{s=0}^{2} w_s q_i^{(s)},\ Q_i^l = \sum_{s=0}^{2} \tilde{w}_s \tilde{q}_i^{(s)},$$

where

$$q_i^{(0)} = \frac{1}{3}\overline{Q}_i + \frac{5}{6}\overline{Q}_{i+1} - \frac{1}{6}\overline{Q}_{i+2},$$

$$q_i^{(1)} = -\frac{1}{6}\overline{Q}_{i-1} + \frac{5}{6}\overline{Q}_i + \frac{1}{3}\overline{Q}_{i+1},$$

$$q_i^{(2)} = \frac{1}{3}\overline{Q}_{i-2} - \frac{7}{6}\overline{Q}_{i-1} + \frac{11}{6}\overline{Q}_i,$$

$$\tilde{q}_i^{(0)} = \frac{11}{6}\overline{Q}_i - \frac{7}{6}\overline{Q}_{i+1} + \frac{1}{3}\overline{Q}_{i+2},$$

$$\tilde{q}_i^{(1)} = \frac{1}{3}\overline{Q}_{i-1} + \frac{5}{6}\overline{Q}_i - \frac{1}{6}\overline{Q}_{i+1},$$

$$\tilde{q}_i^{(2)} = -\frac{1}{6}\overline{Q}_{i-2} + \frac{5}{6}\overline{Q}_{i-1} + \frac{1}{3}\overline{Q}_i,$$

$$w_s = \frac{\alpha_s}{\sum_{p=0}^{2}\alpha_p},\ \alpha_s = \frac{d_s}{(\epsilon+\beta_s)^2},$$

$$\tilde{w}_s = \frac{\tilde{\alpha}_s}{\sum_{p=0}^{2}\tilde{\alpha}_p},\ \tilde{\alpha}_s = \frac{\tilde{d}_s}{(\epsilon+\beta_s)^2}, s = 0,1,2,$$

$$\beta_0 = \frac{13}{12}(\overline{Q}_i - 2\overline{Q}_{i+1} + \overline{Q}_{i+2})^2 + \frac{1}{4}(3\overline{Q}_i - 4\overline{Q}_{i+1} + \overline{Q}_{i+2})^2,$$

$$\beta_1 = \frac{13}{12}(\overline{Q}_{i-1} - 2\overline{Q}_i + \overline{Q}_{i+1})^2 + \frac{1}{4}(\overline{Q}_{i-1} - \overline{Q}_{i+1})^2,$$

$$\beta_2 = \frac{13}{12}(\overline{Q}_{i-2} - 2\overline{Q}_{i-1} + \overline{Q}_i)^2 + \frac{1}{4}(\overline{Q}_{i-2} - 4\overline{Q}_{i-1} + 3\overline{Q}_i)^2,$$

$$d_0 = \tilde{d}_2 = \frac{3}{10},\ d_1 = \tilde{d}_1 = \frac{3}{5},\ d_2 = \tilde{d}_0 = \frac{1}{10},\ \epsilon = 10^{-6}.$$

3.2 Reconstruction of initial subcell flow distributions

When the pointwise variables on both sides of a cell interface are provided, we still need to construct subcell flow distributions inside each control volume as the initial condition for the evaluation of interface gas distribution function. A 3rd-order polynomial inside each cell can be written as

$$V(x) = V_i + S_i^1(x - x_i) + \frac{1}{2}S_i^2(x - x_i)^2, x \in [x_{i-1/2}, x_{i+1/2}],$$

where x_i is the cell center, $x_{i-1/2}$ and $x_{i+1/2}$ are the left and right interfaces of the ith cell, V_i, S_i^1 and S_i^2 are three unknowns. From the three conditions

$$\frac{1}{x_{i+1/2} - x_{i-1/2}}\int_{x_{i-1/2}}^{x_{i+1/2}} = \overline{V}_i,\ V(x_{i-1/2}) = V_i^l,\ V(x_{i+1/2}) = V_i^r,$$

we can get

$$V_i = \frac{3}{2}\overline{V}_i - \frac{1}{4}(V_i^l + V_i^r),$$

$$S_i^1 = \frac{V_i^r - V_i^l}{x_{i+1/2} - x_{i-1/2}},\ S_i^2 = \frac{6[(V_i^l + V_i^r) - 2\overline{V}_i]}{(x_{i+1/2} - x_{i-1/2})^2}.$$

So, the derivatives of $V(x)$ at the cell interface can be easily obtained from the above distribution.

3.3 Reconstruction of a continuous flow distribution across a cell interface

The final flux of GKS depends on the integral solution eq. (16) of an equilibrium state across a cell interface. At the cell interface, the pointwise equilibrium state can be obtained from eq. (15). In order to determine all high-order expansion terms of an equilibrium state across a cell interface, we need to use high-order derivatives of conservative flow variables. Assume, $V_{i+1/2}$ is one of the conservative flow variables, the local expansion is

$$\overline{V}(x) = V_{i+1/2} + \overline{S}_{i+1/2}^1(x - x_{i+1/2}) + \frac{1}{2}\overline{S}_{i+1/2}^2(x - x_{i+1/2})^2$$

$$+\frac{1}{6}\bar{S}^3_{i+1/2}(x-x_{i+1/2})^3+\frac{1}{24}\bar{S}^4_{i+1/2}(x-x_{i+1/2})^4.$$

From the conditions

$$\frac{1}{x_{i+5/2}-x_{i+3/2}}\int_{x_{i+3/2}}^{x_{i+5/2}}=\bar{V}_{i+2},\quad \frac{1}{x_{i+3/2}-x_{i+1/2}}\int_{x_{i+1/2}}^{x_{i+3/2}}=\bar{V}_{i+1},$$
$$\frac{1}{x_{i+1/2}-x_{i-1/2}}\int_{x_{i-1/2}}^{x_{i+1/2}}=\bar{V}_{i},\quad \frac{1}{x_{i-1/2}-x_{i-3/2}}\int_{x_{i-3/2}}^{x_{i-1/2}}=\bar{V}_{i-1},$$

we can determine all $\bar{S}^n,(n=1,2,3,4)$. For the 3rd-order GKS, we only need to keep $\bar{S}^1$ and $\bar{S}^2$ terms. For a uniform mesh, we have

$$\bar{S}^1_{i+/2}=\frac{-\frac{1}{12}(\bar{V}_{i+2}-\bar{V}_{i-1})+\frac{5}{4}(\bar{V}_{i+1}-\bar{V}_i)}{\Delta x},$$
$$\bar{S}^2_{i+1/2}=\frac{-\frac{1}{8}(\bar{V}_{i+2}+\bar{V}_{i-1})+\frac{31}{8}(\bar{V}_{i+1}+\bar{V}_i)-\frac{15}{2}V_{i+1/2}}{(\Delta x)^3},$$

where $\Delta x=x_{i+1/2}-x_{i-1/2}$ for any i. Because all the high-order derivatives will participate in the construction of the local gas evolution in GKS, the kinetic method will not be very sensitive to the interface pointwise values.

4 Numerical examples

For the Euler system, the solutions of WENO-GKS-Euler is compared with the solutions of the WENO-Godunov scheme, where the exact Riemann solver is used for the flux evaluation [14], and a Runge-Kutta multistage method is adopted for achieving a 3rd-order time accuracy. In all comparison, the reconstruction and the CFL number are the same for both WENO-GKS-Euler and WENO-Godunov scheme. We will also test WENO-GKS-NS for viscous solution. The same 5th-order WENO subcell reconstruction for conservative variables is used in all the tests.

4.1 Problems in 1D space

All 1D test cases are about the Euler solutions. In WENO-GKS-Euler, $\alpha=0.0001$ and $\beta=0.0001$ in eq. (21) are used in all 1D test cases except $\beta=0.01$ for the "large density ratio problem". In all calculations, the CFL number is 0.6 for both WENO-GKS-Euler and WENO-Godunov scheme.

4.1.1 The 1D Riemann problem

We consider two Riemann problems here. The initial conditions are the followings.

(a) Riemann problem proposed by Lax in ref. [15] is

$$(\rho,U,p)=\begin{cases}(0.445,0.698,3.528), & 0\leqslant x<50,\\ (0.5,0,0.571), & 50\leqslant x\leqslant 100.\end{cases}$$

(b) Large density ratio problem proposed in ref. [16] is

$$(\rho,U,p)=\begin{cases}(10000,0,10000), & 0\leqslant x<30,\\ (1,0,1), & 30\leqslant x\leqslant 100.\end{cases}$$

Figure 1 shows the solutions from the WENO-GKS- Euler and WENO-Godunov scheme. Both methods work very well for the shock tube problem. Figure 2 shows slight deviation between the WENO-GKS-Euler and WENO-God–unov results. Due to the controlling of numerical dissipation through the parameter β in eq. (21), the WENO-GKS presents a more accurate Euler solutions. For the Euler solutions, theoretically, there is no physical dissipation. But,

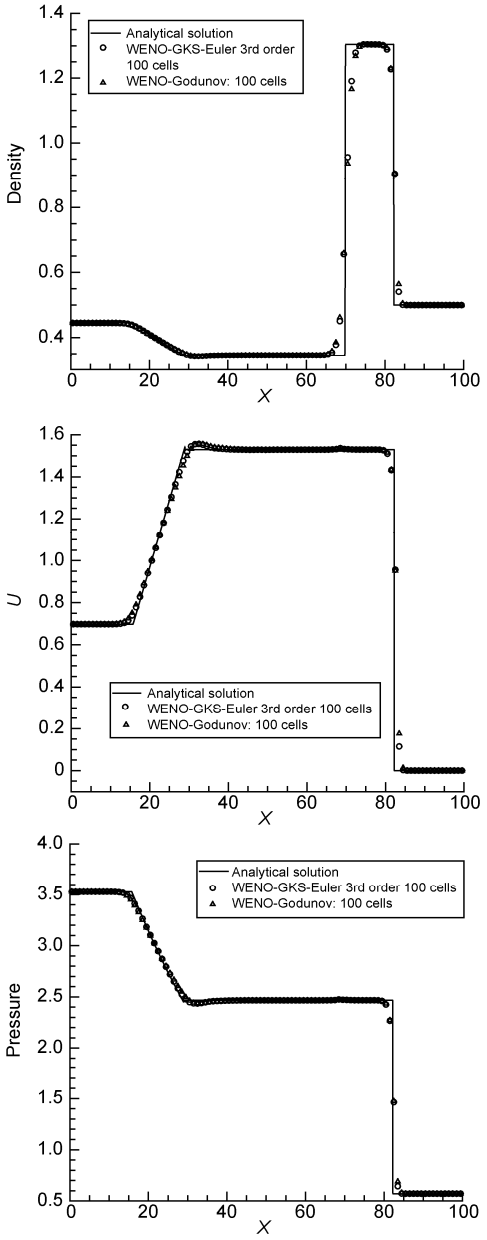

Figure 1 Lax Riemann problem: the density, velocity, and pressure distributions at t = 13 with 100 cells. Circle: the 3rd-order WENO-GKS-Euler scheme. Triangle: WENO-Godunov scheme.

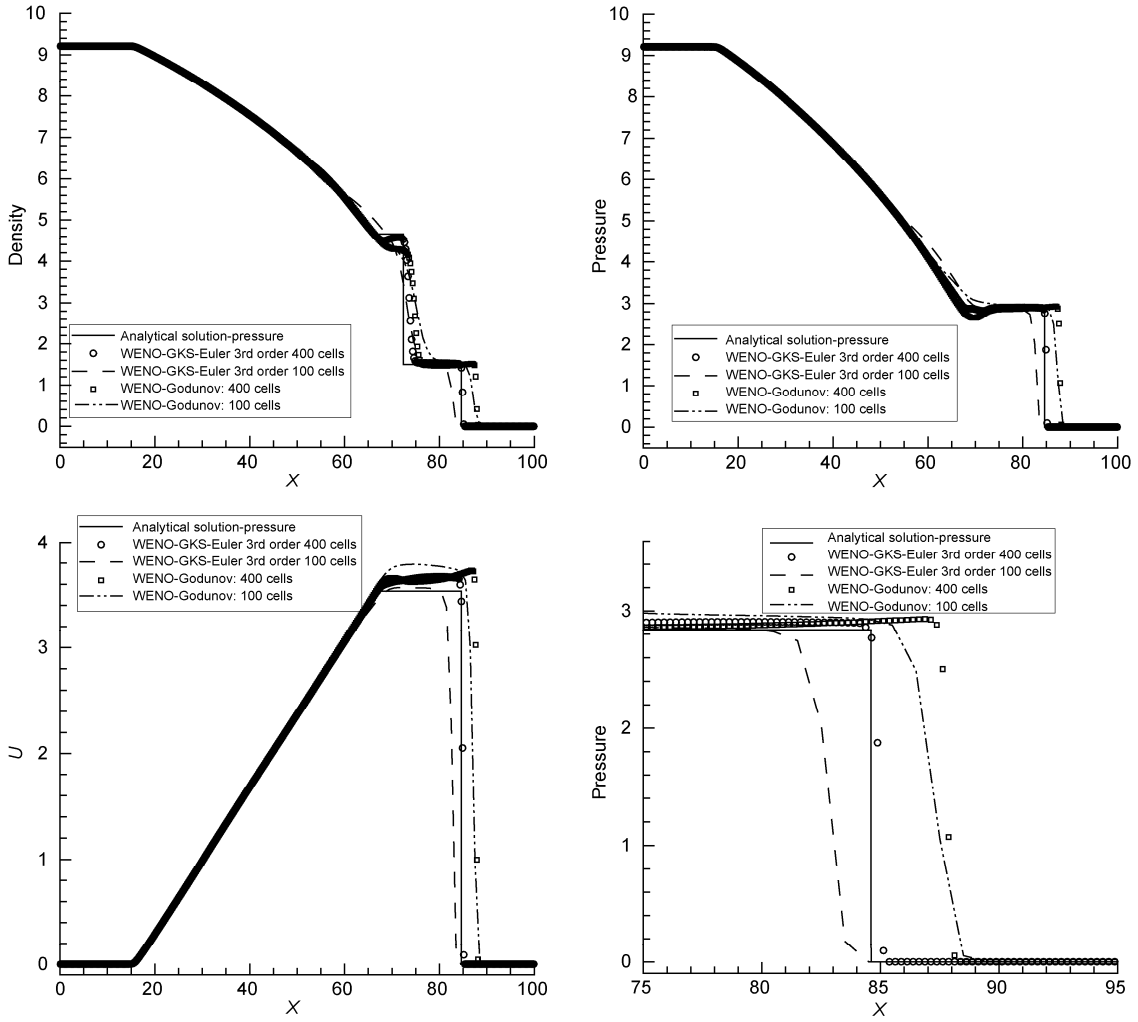

Figure 2 Large density ratio problem: the density, velocity and pressure distributions at t = 12 with 400 and 100 cells. The density and pressure are plotted on a logaritmic scale. The last figure is the enlarged region around the shock front of the pressure distribution.

numerical dissipation is necessary to control the oscillation in the shock region. With the use of the low order dynamic model of the exact Riemann solution, the WENO-Godunov seems to introduce more numerical dissipation than the WENO-GKS-Euler, where a high-order gas evolution model is used.

4.1.2 Woodward-Colella blast wave problem

The blast wave problem was originally proposed in ref. [17]. The computational domain is [0, 100] with reflected boundary condition on both ends. The initial flow field is stationary with unit density and different pressures

$$p=\begin{cases}1000, & 0\leqslant x<10,\\ 0.01, & 10<x\leqslant 90,\\ 100, & 90<x\leqslant 100.\end{cases}$$

The density and pressure distributions at t = 3.8 with different numbers of cells are shown in Figure 3. The density distribution shows that the WENO-GKS-Euler works a little bit better than the WENO-Godunov method.

4.1.3 Shu-Osher shock acoustic-wave interaction

This problem is the interaction of a moving shock with smooth density fluctuation [2]. The computational domain is [−5, 5] and the flow field is initialized as

$$(\rho,U,p)=\begin{cases}(3.857134,2.629369,10.33333), & x<-4,\\ (1+0.2\sin(5x),0,1), & x\geqslant -4.\end{cases}$$

The computed density profile at t = 1.8 is shown in Figure 4. Again, the WENO-GKS-Euler works a little bit better than the WENO-Godunov. A small overshoot happens around the local extremes in the results of WENO-GKS-Euler.

Based on the 1D Euler solutions, we can conclude that WENO-GKS-Euler is as good as the WENO-Godunov scheme in all the cases. Due to the less numerical dissipation, the BGK-Euler solutions may be closer to analytical Euler solutions than those calculated by the exact Riemann solver in some tough cases.

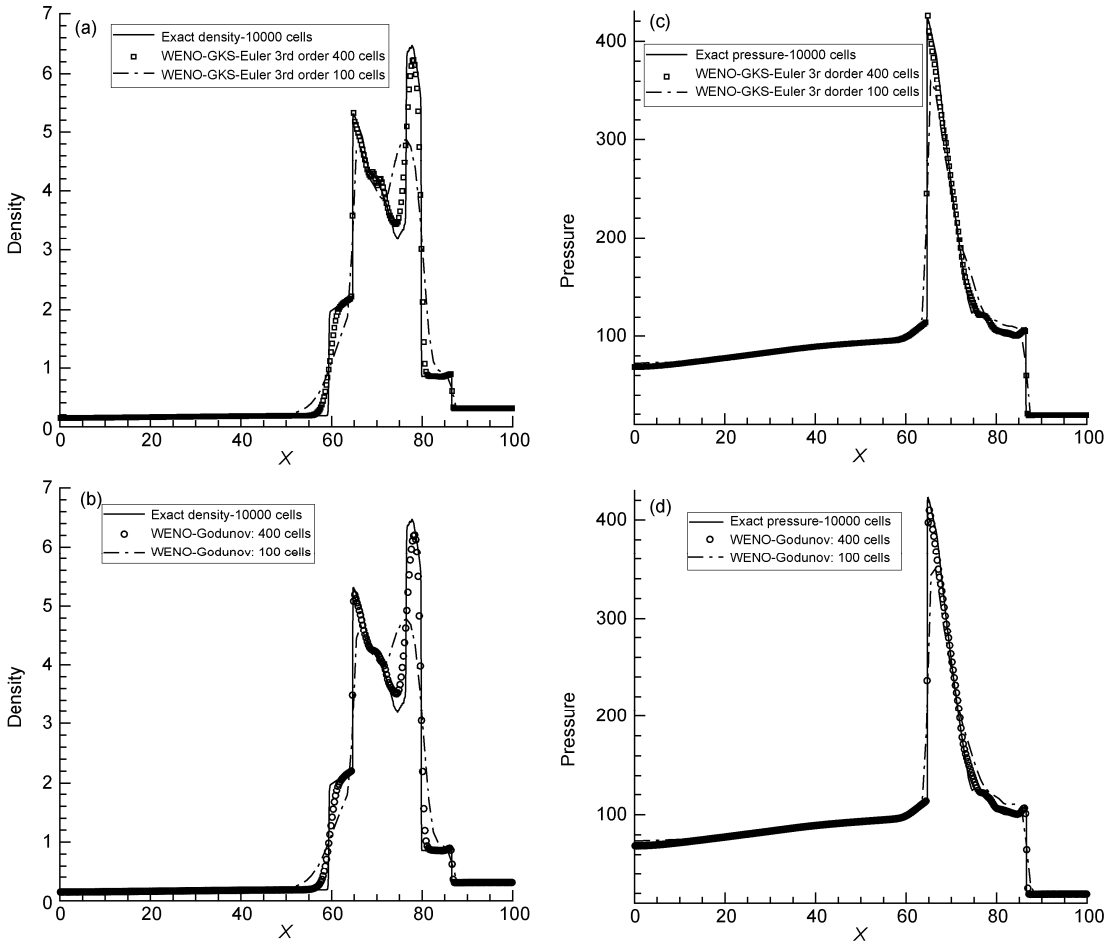

Figure 3 Woodward-Colella blast wave problem: the density and pressure distributions at t = 3.8 with 400 and 100 cells. (a) and (c): the 3rd-order WENO-GKS-Euler. (b) and (d): WENO-Godunov scheme.

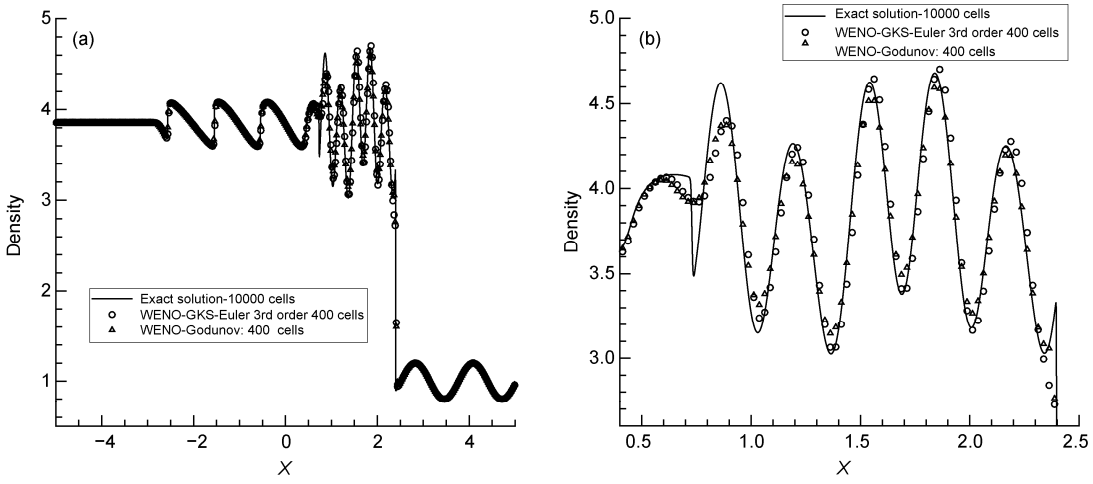

Figure 4 Shu-Osher shock acoustic-wave interaction: the density distribution at t=1.8 with 400 cells. (b) is the enlarged region with high frequency oscillation in (a).

4.2 Problems in 2D space

The 2D cases are all about the NS solutions. It is not easy to physically extend the WENO-Godunov scheme to the NS system because of the lack of the "Riemann" solution for the NS equations. Therefore, we only use WENO-GKS-NS here. The collision time is defined in eq. (22). CFL number 0.3 is used for the first two cases. Because of the existence

of the strong shock, $\beta = 1000.0$ is used for Mach 3 step problem, and $\beta = 1.0$ for the Shock vortex interaction case. For the cavity simulation, the flow is smooth, there is no reason to introduce the numerical dissipation, so $\beta = 0.0001$ and CFL number 0.5 are used.

4.2.1 Mach 3 step problem

The Mach 3 step problem was first proposed by Woodward and Colella in ref. [17]. The computational domain is $[0,3]\times[0,1]$. A step with height 0.2 is located at $x = 0.55$. The upstream velocity is $(U,V) = (3,0)$. The adiabatic slip Euler boundary condition is implemented at all boundaries. The results for different Reynolds numbers (*Re*) and different numbers of cells are given in Figures 5 and 6.

Figure 5 shows the NS solutions at different Reynolds numbers. The combination of the 5th-order WENO reconstruction and the 3rd-order GKS-NS flux presents an accurate solution. Because of the use of both numerical and the physical collision times, an oscillation free transition can be obtained around a shock with different mesh sizes (see Figure 6).

4.2.2 Shock vortex interaction

This is a problem which was presented in refs. [18, 4]. On the computational domain $[0,2]\times[0,1]$, a stationary shock front is positioned at $x = 0.5$. The left upstream state is $(\rho,U,V,p) = (M^2,\sqrt{\gamma},0,1)$, where γ is the specific heat ratio and M is the Mach number. A small vortex is a perturbation on the mean flow with the velocity (U,V), temperature $(T = p/\rho)$ and entropy $\left(S = \ln\frac{p}{\rho^\gamma}\right)$, where the perturbation is

$$\tilde{U} = \kappa\eta\, e^{\mu(1-\eta^2)}\sin\theta,\ \tilde{V} = -\kappa\eta\, e^{\mu(1-\eta^2)}\cos\theta,$$

$$\tilde{T} = -\frac{(\gamma-1)\kappa^2 e^{2\mu(1-\eta^2)}}{4\mu\gamma},\ \tilde{S} = 0,$$

where $\eta = r/r_c$, $r = \sqrt{(x-x_c)^2+(y-y_c)^2}$, (x_c, y_c) =(0.25, 0.5) is the center of the vortex, κ and μ control the strength and decay rate of the vortex, and r_c is the critical radius. Here, we choose $\kappa = 0.3$, $r_c = 0.05$ and $\mu = 0.204$.

In the tests, the gas is a diatomic molecule with $\gamma = 1.4$. The number of cells is 200×101. The reflected boundary condition is used on the top and bottom boundaries. The evolution solution at *Re*=1.0×10^5 is given in Figure 7. The pressure distributions for different Reynolds numbers at *t* =

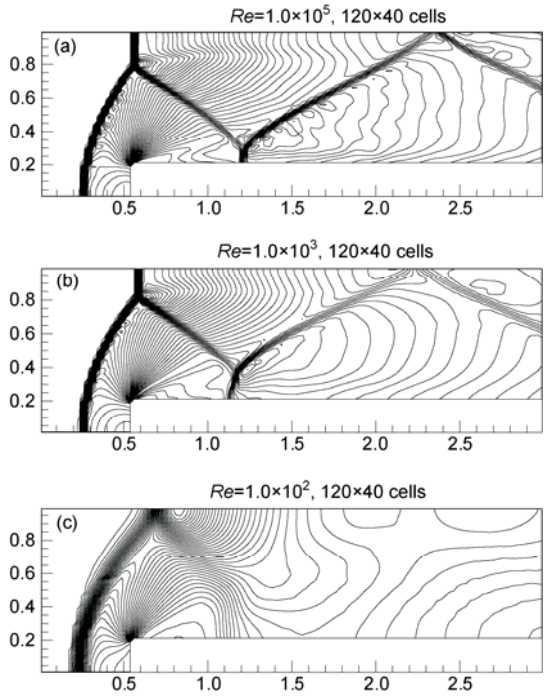

Figure 5 Mach 3 step problem: the density distribution for different Reynolds numbers (*Re*) at *t* = 4.0 with 120×40 mesh points by the 3rd-order WENO-GKS-NS. In each figure, there are 50 contours from 0.5 to 5.

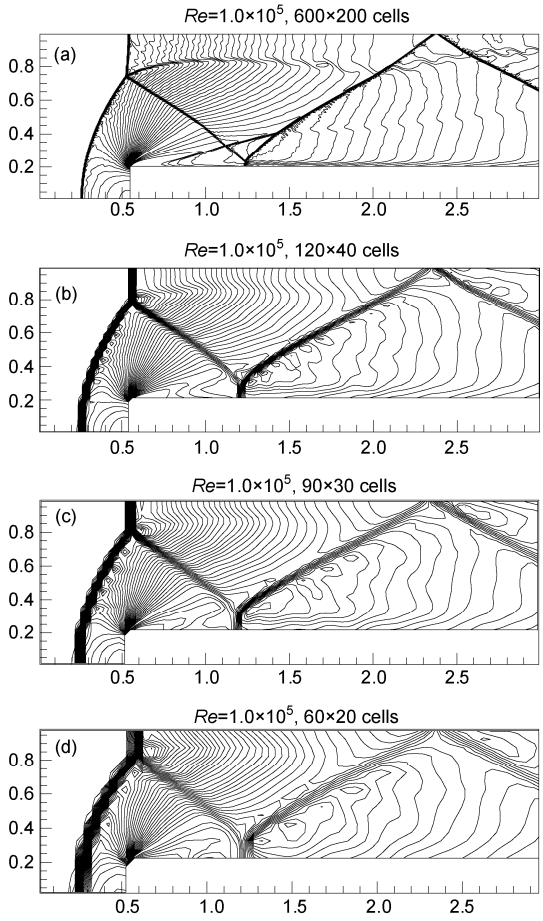

Figure 6 Mach 3 step problem: the density distribution for different number of mesh points at *t*=4.0 with *Re*=1.0×10^5 by the 3rd-order WENO-GKS-NS. In each figure, there are 50 contours from 0.5 to 5.

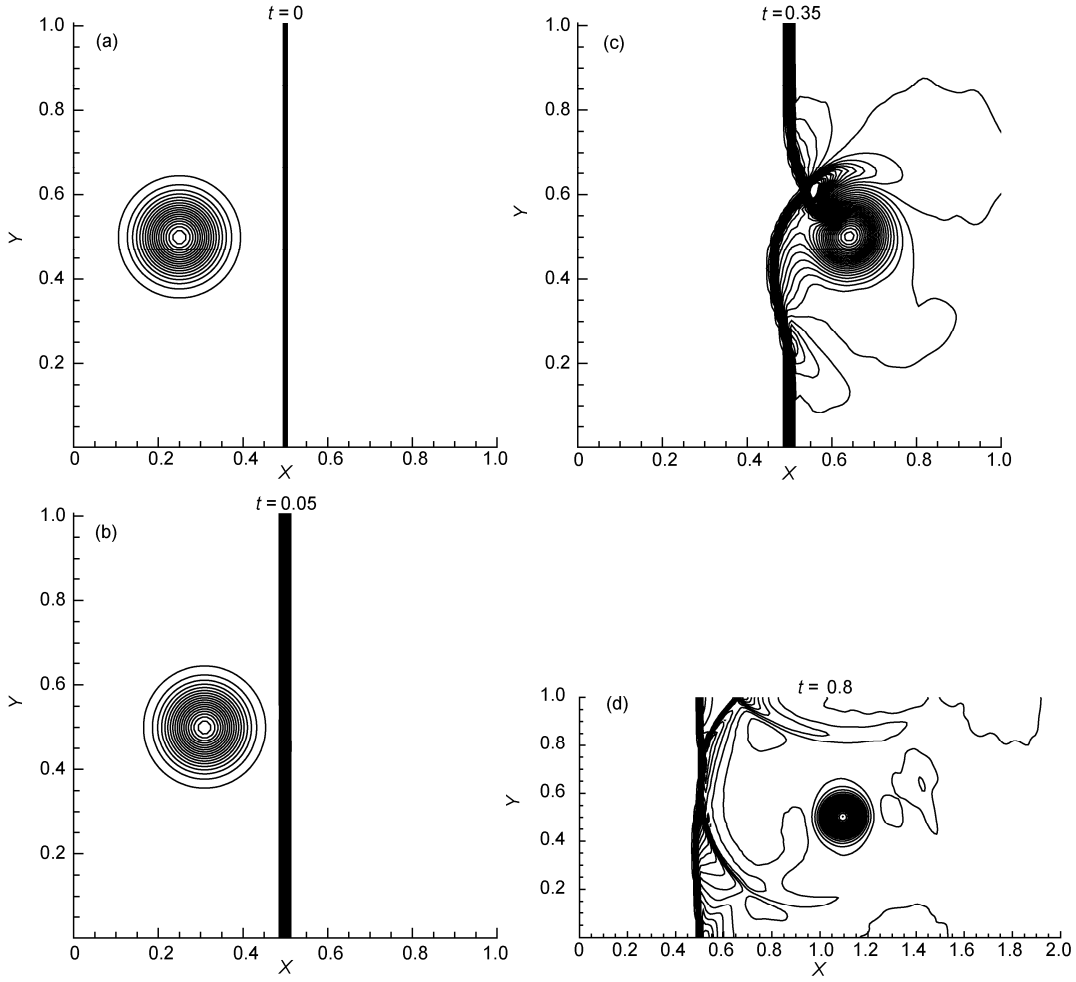

Figure 7 Shock vortex interaction: the pressure distributions at different times with Re=1.0×10^5 by the 3rd-order WENO-GKS-NS. In each figure, there are 60 contours from 0.8 to 1.4.

0.6 are shown in Figure 8. The detailed pressure and velocity distributions at different Reynolds numbers at t =0.8 along the horizontal symmetric line y = 0.5 are shown in Figure 9.

4.2.3 Low speed cavity flow

The cavity flow at low Mach number is a standard test case for validating incompressible or low speed NS flow solvers. Since the benchmark solution is from incompressible NS equations, in order to avoid kinematic dissipation [19–21], most simulations in the past are based on either the methods for the incompressible equations or the artificial compressibility methods, where a continuous initial reconstruction across a cell interface is assumed. However, here we are going to use the same shock capturing WENO-GKS for the cavity simulation. This is a challenge for any shock capturing NS flow solver, because the cell interface discontinuity may generate a large amount numerical dissipation. The flow simulated has a Mach number 0.3 at the Reynolds number 1000 and $\gamma = 1.4$. The fluid is bounded by a unit square and is driven by a uniform translation of the top boundary. All the boundaries are isothermal and nonslip. Figure 10 shows the calculated stream traces with 64×64 and 32×32 mesh points. The results of U-velocity and pressure along the vertical symmetric line at x = 0.5, and V-velocity and pressure along the horizontal symmetric line at y = 0.5 are shown in Figure 11. The benchmark solution is from ref. [22]. And the reference solution for pressure is from ref. [23]. As shown in Figure 11, even with 64×64 cells, the simulation results from WENO-GKS-NS match the exact solutions very well. This can be hardly achieved for a shock capturing scheme, especially for the schemes based on the directional splitting method.

4.3 Accuracy and computation time

We test the order of accuracy of the WENO-GKS in the following two cases.

Case 1. Advection of density perturbation.

The initial condition is set to be $\rho(x) = 1 + 0.2\sin(\pi x)$, $U(x) = 1$ and $p(x) = 1$. The computational domain is [0, 2]. The periodic boundary condition is adopted and thus

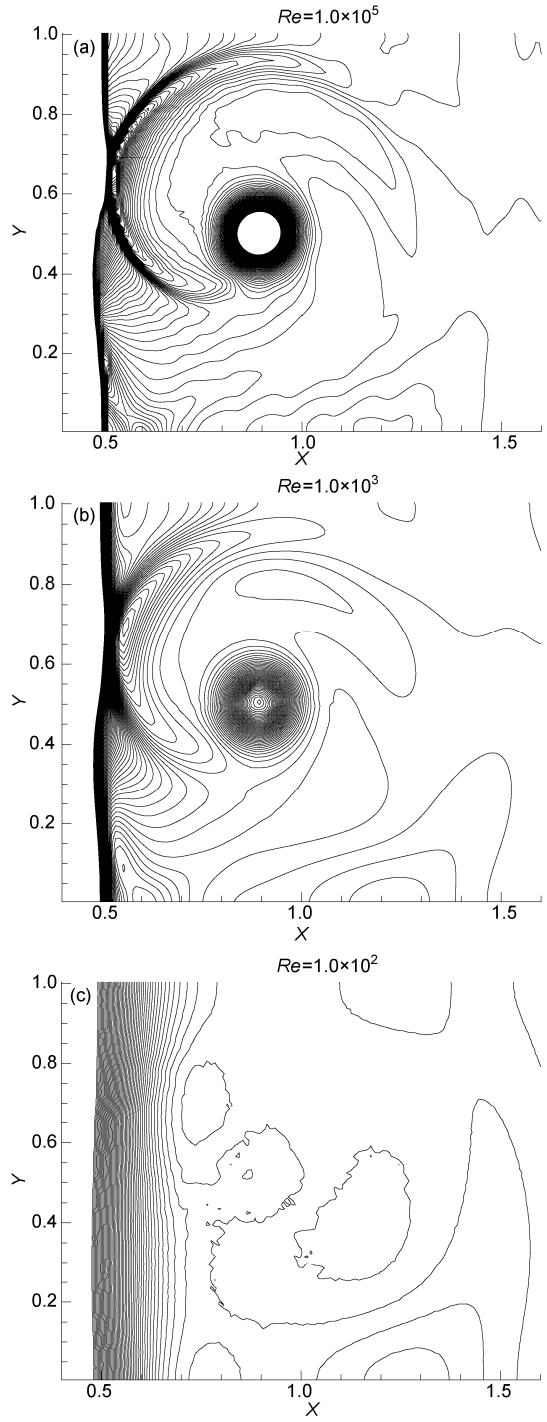

Figure 8 Shock vortex interaction: the pressure distribution for different Reynolds numbers at t=0.6 by the 3rd-order WENO-GKS-NS. In each figure, there are 90 contours from 1.1 to 1.37.

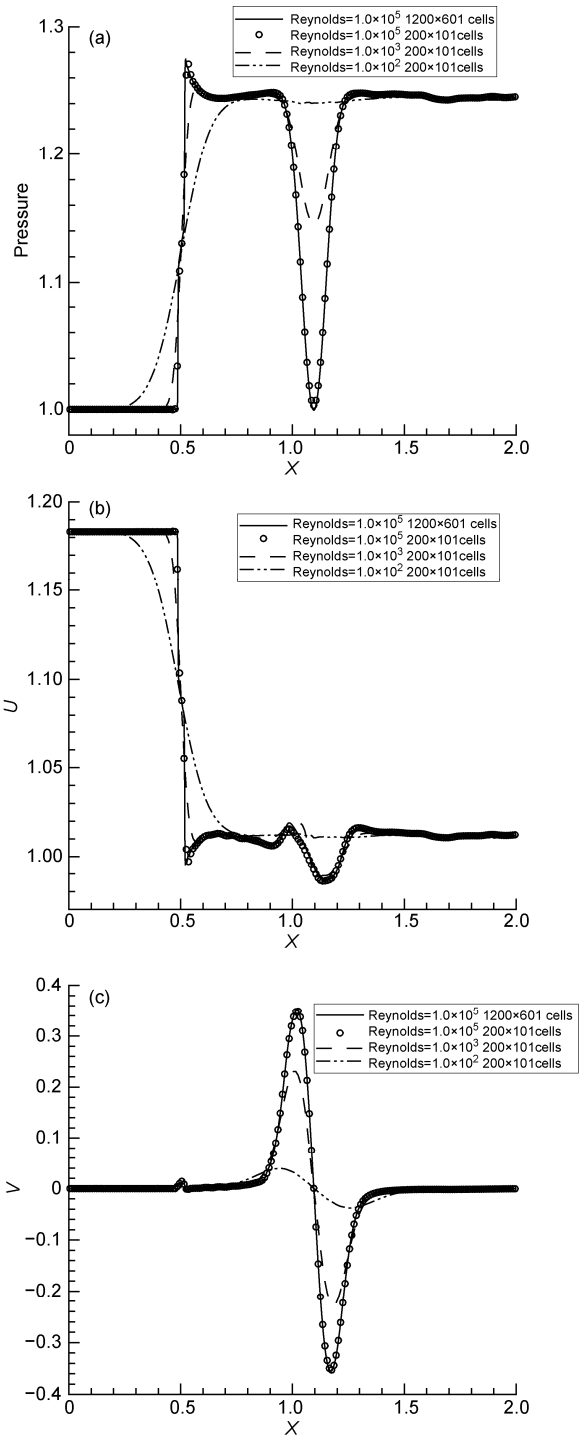

Figure 9 Shock vortex interaction: the pressure and velocity (U, V) along the horizontal symmetric line y=0.5 for different Reynolds numbers at t=0.8 by the 3rd-order WENO-GKS-NS.

the analytic solution is $\rho(x,t)=1+0.2\sin(\pi(x-t))$, $U(x, t)$=1 and $p(x, t)$=1. In the WENO-GKS-Euler, α=1.0×10^{-10} and β=1.0×10^{-3} for the numerical collision time in eq. (21). The error of the density is computed at t=2. Firstly, we test the space accuracy. In this test, CFL=0.1. The error and convergence rate of the density are shown in Table 1. Even with a 3rd-order gas evolution model, the 5th-order WENO reconstruction seems to make the WENO- GKS scheme have good order of accuracy.

For the time accuracy, we test it for the different CFL numbers with the uniformly 800 cells. The results are shown in Table 2. The 3rd-order time accuracy can be achieved by GKS due to the fully coupled space and time evolution.

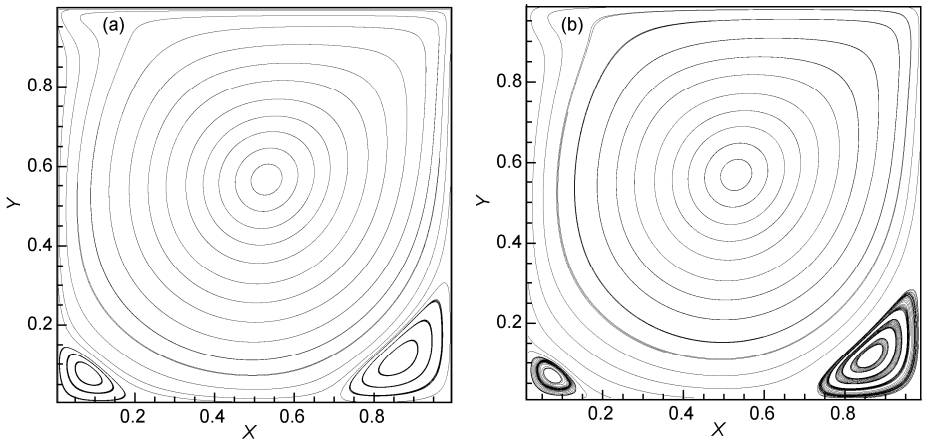

Figure 10 Cavity flow: the streamlines at Re = 1000 calculated by the 3rd-order WENO-GKS-NS. (a) 65×65 cells; (b) 33×33 cells.

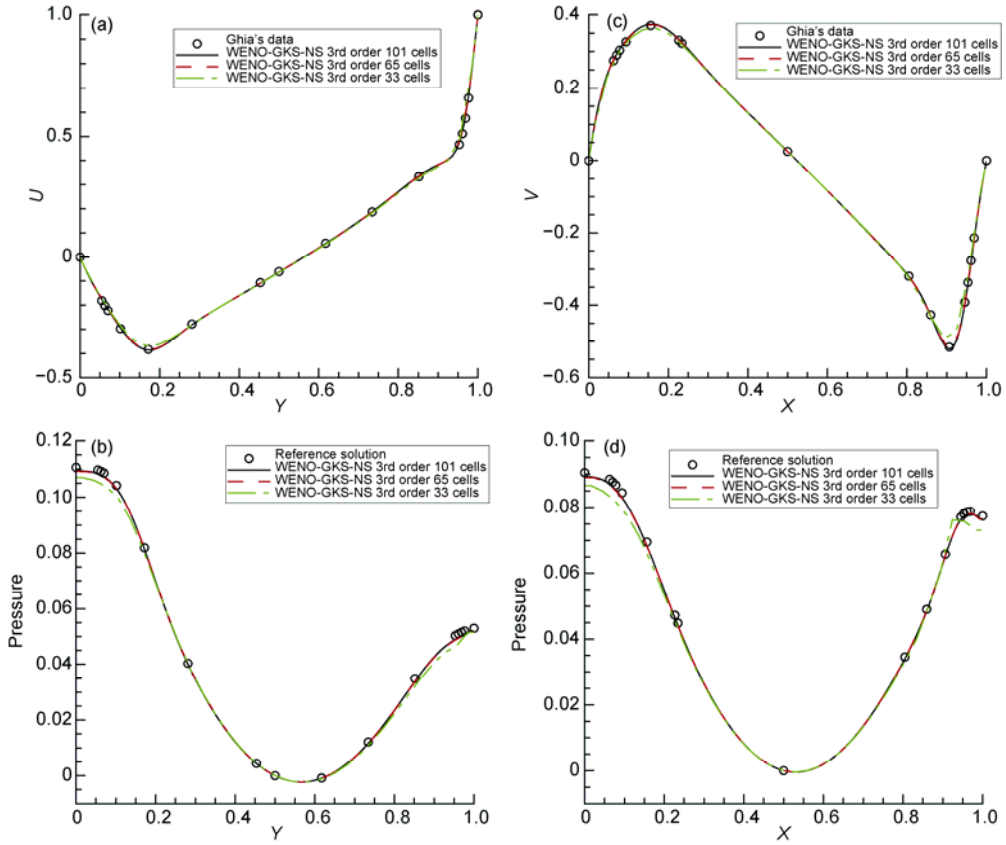

Figure 11 Cavity flow: U and pressure distributions along the vertical symmetric line at x = 0.5 and V and pressure distributions along the horizontal symmetric line at y = 0.5 with Re=1.0×10^3 and Mach number 0.3 by the 3rd-order WENO-GKS-NS. The benchmark velocity solution is from ref. [22]. The reference pressure is from ref. [23]. (a) and (b) Along the vertical symmetric line at x = 0.5; (c) and (d) along the horizontal symmetric line at y = 0.5.

Table 1 Space accuracy test for advection of density perturbation by WENO-GKS

Grid	L_∞ error	Order	L_1 error	Order	L_2 error	Order
400	1.3041×10^{-10}	5.0072	7.4726×10^{-11}	4.9106	8.3469×10^{-11}	4.9250
200	4.1978×10^{-9}	5.1508	2.2494×10^{-9}	4.9791	2.5362×10^{-9}	4.9906
100	1.4902×10^{-7}	5.0447	7.0935×10^{-8}	4.9986	8.0582×10^{-8}	5.0389
50	4.9200×10^{-6}	4.8398	2.2673×10^{-6}	5.0468	2.6500×10^{-6}	5.0443
20	4.1499×10^{-4}	4.3064	2.3112×10^{-4}	4.3670	2.6952×10^{-4}	4.3152
10	8.2093×10^{-3}	–	4.7681×10^{-3}	–	5.3641×10^{-3}	–

Table 2 Time accuracy test for advection of density perturbation by WENO-GKS

CFL (average time step)	L_∞ error	Order	L_1 error	Order	L_2 error	Order
CFL=0.2 (Δt = 2/9292)	1.746×10^{-11}	2.895	1.196×10^{-11}	2.811	1.313×10^{-11}	2.827
CFL=0.4 (Δt = 2/4646)	1.299×10^{-10}	2.996	8.404×10^{-11}	2.968	9.318×10^{-11}	2.971
CFL=0.6 (Δt = 2/3098)	4.375×10^{-10}	2.997	2.797×10^{-10}	2.987	3.106×10^{-10}	2.987
CFL=0.8 (Δt = 2/2323)	1.036×10^{-9}	–	6.609×10^{-10}	–	7.340×10^{-10}	–

Case 2. Isentropic periodic vortex propagation.

This is a test for the Euler solutions as well. It is a very good test case for the accuracy of high-order schemes (see ref. [13]). The initial condition is given by

$$(U(x,x,0),V(x,y,0)) = (1,1)+\frac{\kappa}{2\pi}\mathrm{e}^{0.5(1-r^2)}(-\overline{y},\overline{x}),$$

$$T(x,y,0) = 1-\frac{(\gamma-1)\kappa^2}{8\gamma\pi^2}\mathrm{e}^{1-r^2}, S(x,y,0) = 1,$$

where the temperature T and the entropy S are related to the density ρ and the pressure p by

$$T = \frac{p}{\rho},\ S = \frac{p}{\rho^\gamma},$$

and $(\overline{x},\overline{y}) = (x-5, y-5)$, $r^2 = \overline{x}^2+\overline{y}^2$, and the vortex strength $\kappa = 5$. The computational domain is [0,10]× [0,10]. The periodic boundary condition is used at both directions. The exact solution is the initial condition convected with the velocity (1,1). The error of the density is computed at t=10, namely after one time period. The data in Table 3 show that the WENO-GKS has a 3rd-order accuracy in 2D case.

The numerical results of the 3rd-order WENO-GKS have been compared with those of the WENO-Godunov scheme in Section 4.1 for Euler solutions. In Table 4, we compare the computation time of different schemes for some 1-D test cases. Since the WENO-Godunov scheme must use the Runge-Kutta time stepping to get time accuracy, it needs to repeat the reconstruction and calculation of fluxes three times within a time step in order to get a 3rd-order time accuracy. Even though the calculation of flux by the WENO-GKS is much more complicated, the computation time is still affordable.

Furthermore, in 2D cases the WENO-Godunov method needs reconstruction and calculates fluxes at each Gaussian integration point along a numerical cell interface in order to keep the high-order accuracy in tangential direction [24]. The work load of the 2D case is quadrupled using the 3rd-order WENO-Godunov scheme in comparison with the 1D case. However, the WENO-GKS directly uses the higher order derivatives. The flux along the interface in the tangential direction can be evaluated analytically. For the WENO-GKS, there is no need to reconstruct and calculate flux many times and at many points within a time step. Also, for the NS solutions, the WENO-Godunov needs to discretize additional viscous and heat conduction terms. However, for the WENO-GKS-Euler and WENO-GKS-NS, the same initial reconstruction can be used. So, we can expect that in 2D and 3D cases the WENO-GKS will become more competitive in terms of efficiency.

5 Conclusions

In this paper, the WENO reconstruction and the gas-kinetic gas evolution model have been combined in the development of a high-order WENO-GKS scheme for the Euler and Navier-Stokes solutions. Many numerical tests have been used to validate the newly developed scheme. The performance of the WENO-GKS and WENO-Godunov methods is compared. The accuracy of WENO-GKS and WENO-Godunov is comparable in 1D test cases. The performance

Table 3 Accuracy test for isentropic periodic vortex propagation by WENO-GKS

Grid	L_∞ error	Order	L_1 error	Order	L_2 error	Order
160	1.4623×10^{-4}	3.3187	1.4062×10^{-5}	2.7553	2.3348×10^{-5}	2.9730
80	1.4593×10^{-3}	4.1410	9.4961×10^{-5}	4.0237	1.8336×10^{-4}	4.2697
40	2.5739×10^{-2}	3.0280	1.5442×10^{-3}	2.8164	3.5360×10^{-3}	2.9508
20	2.0999×10^{-1}	–	1.0879×10^{-2}	–	2.7343×10^{-2}	–

Table 4 Computation time

CPU time (s)	WENO-GKS(3rd order)	WENO-Godunov
Large density ratio (400 cells)	3.8532	1.7160
Large density ratio (100 cells)	0.2184	0.1560
Blast wave (400 cells)	8.8765	3.8220
Shock acoustic-wave interaction (400 cells)	3.6348	1.7004

of WENO-GKS-NS for viscous solution is outstanding. Because of the introduction of both numerical and physical particle collision times, the NS solution obtained by the WENO-GKS-NS method is very accurate, stable and robust. The mesh size effect has been reduced to a minimum level in the capturing of both crisp shock front transition and smooth viscous solution. GKS provides a high-order gas evolution model with a coupled multidimensional space and time flow evolution. In the multidimensional case, a direct integration of the flux transport in the normal direction along a cell interface can be obtained explicitly. The construction of high-order CFD method is on the early stage of development. With the search of short stencil and high order accuracy, the use of high-order dynamical evolution model may become necessary. Otherwise, we have to generate more governing equations in the weak form for the update of additional degree of freedom.

This work was supported by Hong Kong Research Grant Council (Grant No. 621011) and HKUST research fund (Grant No. SRFI11SC05).

1 Harten A, Engquist B, Osher S, et al. Uniformly high order essentially non-oscillatory schemes III. J Comput Phys, 1987, 71: 231–303
2 Shu C W, Osher S. Efficient implementation of essentially nonoscillatory shock-capturing schemes II. J Comput Phys, 1989, 83: 32–78
3 Liu X D, Osher S, Chan T. Weighted essentially non-oscillatory schemes. J Comput Phys, 1994, 115: 200–212
4 Jiang G S, Shu C W. Efficient implementation of weighted ENO schemes. J Comput Phys, 1996, 126: 202–228
5 Xu K. Gas-Kinetic Schemes for Unsteady Compressible Flow Simulations. von Karman Institute report, Belgium, March 1998
6 Xu K. A gas-kinetic BGK scheme for the Navier-Stokes equations, and its connection with artificial dissipation and Godunov method. J Comput Phys, 2001, 171: 289–335
7 Ohwada T, Fukata S. Simple derivation of high-resolution schemes for compressible flows by kinetic approach. J Comput Phys, 2006, 211: 424–447
8 Bhatnagar P L, Gross E P, Krook M. A Model for collision processes in gases I: Small amplitude processes in charged and neutral one-component systems. Phys Rev, 1954, 94: 511–525
9 Li J Q, Li Q B, Xu K. Comparison of the generalized Riemann solver and the gas-kinetic scheme for inviscid compressible flow simulations. J Comput Phys, 2011, 230: 5080–5099
10 Kumar G, Girimaji S S, Kerimo J. WENO-enhanced gas-kinetic scheme for direct simulations of compressible transition and turbulence. J Comput Phys, 2013, 234: 499–523
11 Li QB, Xu K, Fu S. A high-order gas-kinetic Navier-Stokes solver. J Comput Phys, 2010, 229: 6715–6731
12 Ohwada T, Xu K. The kinetic scheme for full Burnett equations. J Comput Phys, 2004, 201: 315–332
13 Shu C W. Essentially non-oscillatory and weighted essentially non-oscillatory schemes for hyperbolic conservation laws. Lecture Notes in Mathematics. Heidelberg: Springer, 1998
14 Toro E. Riemann Solvers and Numerical Methods for Fluid Dynamics. Heidelberg: Springer, 1999
15 Lax P D. Weak solutions of nonlinear hyperbolic equations and their numerical computation. Commun Pure Appl Math, 1954, 7: 159–193
16 Tang H Z, Liu T G. A note on the conservative schemes for the Euler equations. J Comput Phys, 2006, 218: 451–459
17 Woodward P, Colella P. Numerical simulations of two-dimensional fluid flow with strong shocks. J Comput Phys, 1984, 54: 115–173
18 Casper J. Finite-volume implementation of high-order essential ly non-oscil latory schemes in two dimensions. AIAA J, 1992, 30: 2829–2835
19 Su M D, Xu K, Ghidaoui M. Low speed flow simulation by the gas-kinetic scheme. J Comput Phys, 1999, 150: 17–39
20 Xu K, He X Y. Lattice Boltzmann method and gas-kinetic BGK scheme in the low Mach number viscous flow simulations. J Comput Phys, 2003, 190: 100–117
21 Guo Z L, Liu H W, Luo L S, et al. A comparative study of the LBM and GKS methods for 2D near incompressible flows. J Comput Phys, 2008, 227: 4955–4976
22 Ghia U, Ghia K N, Shin C T. High-*Re* solutions for incompressible flow using the Navier-Stokes equations and a multigrid method. J Comput Phys, 1982, 48: 387–411
23 Botella O, Peyret R. Benchmark spectral results on the lid-driven cavity flow. Comput Fluids, 1998, 27: 421– 433
24 Titarev V A, Toro E F. Finite-volume WENO schemes for three-dimensional conservation laws. J Comput Phys, 2004, 201: 238–260